

Emission geometry, radiation pattern, and magnetic topology of the magnetar XTE J1810–197 in its quiescent state

F. Bernardini,^{1,2,3*} R. Perna⁴, E. V. Gotthelf⁵, G. L. Israel², N. Rea⁶, and L. Stella²

¹ *Università degli Studi di Roma “Tor Vergata” Via Orazio Raimondo 18, I-00173 Roma, Italy*

² *INAF – Osservatorio Astronomico di Roma, Via Frascati 33, I-00040 Monteporzio Catone (Roma), Italy*

³ *INAF – Osservatorio Astronomico di Capodimonte, Salita Moiariello 16, I-80131 Napoli, Italy*

⁴ *JILA, Univ. of Colorado, Boulder, CO 80309–0440, USA*

⁵ *Columbia Astrophysics Laboratory, Columbia University, 550 West 120th Street, New York, NY 10027-6601*

⁶ *Institiut de Ciencies de l’Espai (ICE, CSIC-IEEC), 08193, Barcelona, Spain*

ABSTRACT

The return to the quiescent state of the Anomalous X-ray pulsar XTE J1810–197 following its 2003 outburst represents a unique opportunity to probe the surface emission properties of a magnetar. The quiescent emission of XTE J1810–197 is composed of two thermal components, one arising from the whole star surface, and the other from a small warm spot on it. By modeling the magnitude and shape of the pulse profile in narrow spectral bands, we have been able to constrain the physical characteristics and geometrical parameters of the system: the two angles that the line of sight and the spin axis make with respect to the warm spot axis (ψ and ξ respectively), the angular size of the spot, and the overall surface temperature distribution. Our modeling accounts for the general relativistic effects of gravitational redshift and light bending near the stellar surface, and allows for local anisotropic emission. We found that the surface temperature distribution on the neutron star is consistent with the expectations of a dipole magnetic field configuration; the local radiation requires a pencil-beamed emission pattern, suggesting the presence of a magnetized atmosphere. For a typical value of the radius, $R=13$ km, the viewing parameters (symmetric for an interchange between ψ and ξ), range from $\psi = \xi = 38^\circ$ to $(\psi, \xi)=(52^\circ, 29^\circ)$. These angles are consistent with those obtained by modeling the AXP in outburst, with uncertainty contours reduced by a factor of 2.5.

Key words: pulsars: general – stars: neutron – X-rays: individual: XTE J1810–197.

1 INTRODUCTION

XTE J1810–197 is an isolated neutron star (NS) belonging to the class of the Anomalous X-ray Pulsars (AXPs); these objects, together with the Soft Gamma-ray repeaters (SGRs), are believed to be magnetars: isolated neutron stars whose thermal emission and occasional outbursts are powered by their extremely strong magnetic fields (Duncan & Thompson 1992; Thompson & Duncan 1995). Originally one of the thousands of the faint X-ray sources cataloged by ROSAT, the variable nature of XTE J1810–197 was revealed by the outburst of 2003, with its sudden increase in X-ray luminosity by a factor ~ 100 , decaying on a time-scale of years. The source rotation period and its derivative were consequently measured and found to be $P = 5.54$ s and $\dot{P} = 1.1 - 2.1 \times 10^{-11}$ s/s. These timing properties imply a magnetic field $B_{\text{dip}} \sim 3 \times 10^{14}$ G, confirming the magnetar classification of the source (Ibrahim et al. 2004, Gotthelf et al. 2004). The source was monitored repeatedly for more than 7 years with several X-ray observatories, up to the return to quiescence (Gotthelf & Halpern

2005, 2007; Halpern & Gotthelf 2005; Bernardini et al. 2009; Albano et al 2010). These studies presented a unique opportunity to probe the emission mechanisms of a strongly magnetized NS by taking advantage of the flux evolution during its decay. While analysis of phase-averaged spectra alone cannot uniquely distinguish among competing emission models, the addition of the steady change of the spectrum and pulse profile over time greatly increases the diagnostic power.

Perna & Gotthelf (2008) developed a detailed emission model for the energy-dependent pulse profile of XTE J1810–197 following its outburst. This model, which was tailored to the specific surface emission distribution in the post-outburst phase, can take on any viewing geometry, includes the general relativistic effects of light deflection and gravitational redshift, and allows for local anisotropic emission. The application of this model to the first 4 sets of *XMM-Newton* data acquired during the temporal evolution of the flux from XTE J1810–197 following the outburst (September 2003 - September 2004), provided a constraint on the underlying emission geometry and radiation properties of this transient magnetar in its post-outburst phase.

In this paper we present the results of the modeling of the

* E-mail: bernardini@mporzio.astro.it

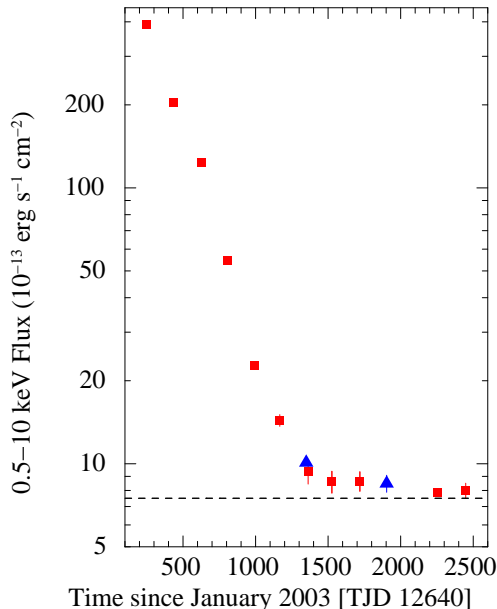


Figure 1. *XMM* (red) and *Chandra* (blue) 0.5–10 keV flux measurements of XTE J1810–197 following its outburst. It is evident from the data that XTE J1810–197 has now reached quiescence. The dashed line represents the X-ray flux level ($\sim 7.5 \times 10^{-13}$ erg cm $^{-2}$ s $^{-1}$) as recorded by *ROSAT*, *Einstein*, and *ASCA* before the outburst onset (Ibrahim et al. 2004, Gotthelf et al. 2004). The analysis presented in the paper is performed over three close *XMM-Newton* pointings represented by the last data point.

spectral and timing data of XTE J1810–197 obtained with 3 combined *XMM-Newton* pointings (September 2009) upon the return of the source to quiescence (see Figure 1, last point). Indeed, our goal here is that of studying the properties of the quiescent emission of this magnetar, which carries information on the surface temperature distribution of the star, and hence on its magnetic topology. We model these data using a modified version of the emission model by Perna & Gotthelf (2008), updated to include: (a) the presence of quiescent emission from the full surface of the star, (b) the changed and reduced emission from the region heated by the outburst.

The new data and its spectral and timing analysis is reported in §2. In §3, we discuss the properties of the quiescent emission. The theoretical emission model is described in detail in §4, and the results of its application to the data are given in §5, following with a discussion in §6.

2 OBSERVATIONS

The quiescent state of the source was observed by *XMM-Newton* during three consecutive close pointings (18 days total time span) in 2009, on September 5, 7, 23 for 19, 18, 12 ks, respectively. All the observations were performed with the PN instrument (Strüder et al. 2001) in large window mode, with the medium filter applied, and the MOS 1 and MOS 2 instruments (Turner et al. 2001) in small window mode, with the use of the medium and thin filter, respectively. The PN resolution time with this configuration is 47.6 ms while the MOS1/2 resolution time is 0.3 s. Data were processed with SAS version 10.0.0, using the updated calibration files (CCF) available in August 2010. Standard data screening criteria were applied in the extraction of scientific products. Time window criteria were used for removing time intervals contaminated by solar flares. A total of 48 ks of good exposure time was obtained. Pho-

ton arrival times were converted into barycentric dynamical times (TBD) using the SAS tool `barycen` and the milliarcsec radio position of Helfand et al. (2007): RA=18 h 09 m 51 s .0870, Dec=-19 $^\circ$ 43' 51''.931 (J2000).

Source photons were extracted from a centered circular region of radius 55'' containing 90% of the source counts. For both the timing and spectral analysis we extracted the background from the same PN or MOS CCD where the source lies using a circular region of the same size as that of the source. In the following analysis, we combine the three PN spectra collected by *XMM-Newton* over an interval of 18 days, after verifying that the individual spectra were consistent with each other within the uncertainties. The spectra were binned to have at least 30 counts per fitting channel to insure adequate fit statistics.

For each observation and instrument we extracted and summed data into four energy bands (following Perna & Gotthelf, 2008): 0.5–1, 1–1.5, 1.5–2 and 2–3 keV. Lightcurves were generated at the minimum allowed bin time of 0.3 s. We phase connected the three multi-instrument lightcurves using the phase-fitting technique outlined in Dall’Osso et al. (2003). The timing solution, referred to epoch MJD 54079, includes only one term, the rotation period, which was found to be $P = 5.5406556 \pm 2 \times 10^{-7}$ s. The brief span of the observations did not allow for a spin-down measurement, but only for a 3σ upper limit of $\dot{P} \leq 9 \times 10^{-12}$ s/s (consistent with the value $\dot{P} = 0.8 - 1.0 \times 10^{-11}$ s/s reported by Camilo et al. 2007 for the 2006–2007 observation period). The pulse profile at different energy bands was determined by means of the P value reported above. The profile was found to be nearly sinusoidal and energy independent in analogy with earlier epochs (Halpern and Gotthelf 2005; Bernardini et al. 2009).

3 PROPERTIES OF THE QUIESCENT EMISSION

Halpern & Gotthelf (2005) and Gotthelf & Halpern (2005) showed that the post-outburst spectrum was composed of a multi-blackbody (BB) made up of two thermal components, which they interpreted as a warm ring surrounding a hot spot. Bernardini et al. (2009) further showed evidence for a third, cooler thermal component consistent with emission from the whole surface of the star. The recorded outburst flux was a factor ~ 100 times higher than in the quiescent state. They also found that, while the intensity of the emission from the whole NS surface was constant during the outburst (and equal to the one recorded in quiescence), the flux from the two hotter regions decreased exponentially with time (on a timescale $\tau \sim 1$ yr). Spectral analysis showed that the warm and the hot regions were shrinking with time, and the total luminosity of the star was consequently declining towards the quiescent level. When the source eventually returned to quiescence, its spectrum was fully consistent with that recorded by ROSAT before the outburst. More in detail, the quiescent flux was found to be composed of a cool BB component consistent with emission from the whole NS surface (for the best estimated distance value of ~ 3.3 kpc; Camilo et al. 2006, Minter et al. 2007, Durant & van Kerkwijk 2006), and a warmer BB emission coming from a small, residual spot. The quiescent spectrum of the source is therefore composed by two BB only (see Figure 2 left panel). It should however be noted that the quiescent spectrum also displays a statistically significant ($\sim 5\sigma$) absorption feature around 1.1 keV. This feature, discussed in Bernardini et al. (2009), is of unknown origin. It could be a proton cyclotron line if the magnetic field is $B = 2.2 \times 10^{14}$ G (an electron cyclotron line would imply a B field about 2000 times weaker, out of the

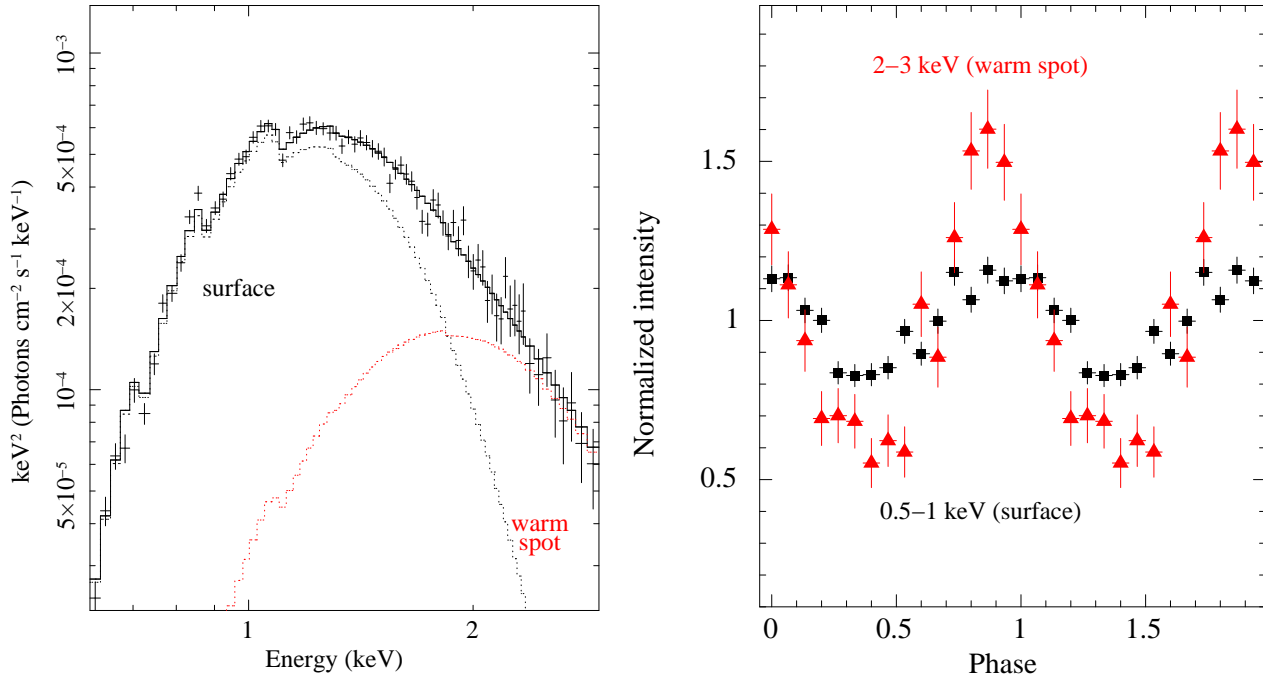


Figure 2. *Left panel:* The quiescent spectrum of XTE J1810–197 modeled with a 2BB model with the softer component associated with the entire surface and the hotter component, with a higher level of PF, associated with a localized warm spot. *Right panel:* Pulse profile of the surface component (black square) compared to the warm spot pulse profile. Both profiles show a peak at the same phase interval ($\phi \sim 0.85$).

magnetar range). In our spectral fits, the feature is modeled with an edge. We have verified that, within uncertainties, the absorption depth (τ_c) at the energy threshold (E_c) is independent of phase, and of magnitude $\langle \tau_c \rangle = 0.32 \pm 0.02$. Hence the presence of this feature is not expected to affect the results from the timing analysis and is not included therein. Such a feature is however included in all spectral fits in the present work.

Since XTE J1810–197 has now returned to quiescence, the temperature distribution on the star surface reflects the overall magnetic field distribution, as the conductivity is enhanced along magnetic field lines. For most AXPs, the high level of pulsed fraction cannot be produced by a temperature distribution following a dipole magnetic field (De Deo, Psaltis & Narayan 2000). In the case of XTE J1810–197, on the other hand, the low level of pulsed fraction of the soft X-ray bands could be the result of such a field configuration, which we hence adopted as our starting point. A determination of the XTE J1810–197 surface temperature distribution would allow to unveil its magnetic field configuration.

The spectral component corresponding to the cold NS surface easily dominates the emission below 1 keV, while the emission corresponding to the warm spot dominates over 2 keV (see figure 2 left panel). Our first goal was the localization on the star surface of the warm spot with respect to the maximum intensity of the cooler surface emission (corresponding to the magnetic axis). Note that, albeit the NS surface is expected to have a temperature gradient, however, due to the limited S/N ratio of the spectral data, it can only be identified as a single BB in the spectral analysis (i.e. the colder one). The pulse profiles of the two BB components were consequently generated separately by taking into account only photons emitted in the 0.5–1 keV and 2–3 keV energy bands respectively. The result of this test shows (see figure 2 right panel) that the maximum of the pulsed emission coming from the NS surface remains in phase with the maximum in the hardest energy band, dominated

by the warm spot. Therefore, one the two (warmer) regions on the star surface associated with the magnetic poles must be very close to the center of the warm spot. It is important to note that, while the highest energy bands (dominated by the emission from the single hot spot), naturally produce a single-peaked profile, in the lowest energy band, dominated by the surface emission (characterized by two symmetrically opposed warmer regions), a single peak profile is expected only for geometries for which only one pole is visible as the pulsar rotates (e.g. Page 1995).

These results and considerations represent the basis to develop a model that allows us to predict the energy-dependent pulsed fraction and pulse profile, and use it to determine, for different values of the NS radius, the viewing geometry and beaming pattern of the emitted radiation that best match the observations. The model is described in detail in the next section.

4 MODELING THE SPECTRUM AND THE PULSE PROFILE OF XTE J1810–197 IN QUIESCENCE

Following the motivations given in the previous section, the local temperature distribution, $T_{\text{th}}(r, \theta)$ (in spherical coordinates), on the surface of XTE J1810–197 is modeled as expected from thermal cooling under the influence of a dipole magnetic field (Heyl & Hernquist 1998; see also Perna et al. 2001):

$$T_{\text{th}}(\theta, \phi) = T_p \left[\frac{4 \cos^2 \theta_p}{3 \cos^2 \theta_p + 1} (0.75 \cos^2 \theta_p + 0.25)^{0.2} \right], \quad (1)$$

where T_p is the pole temperature and θ_p is the angle between the radial direction at position (θ, ϕ) on the surface of the star and the magnetic pole.

Superimposed to the emission from the whole (cold) surface of the star is the emission from a small (hot) spot, whose axis coin-

cides with the dipole axis. The mathematical description of the spot on the rotating surface (of temperature T_h and angular radius β_h) follows the theory developed by Pechenick et al. (1993) with some generalizations presented by Perna & Gotthelf (2008). If ξ defines the angle between the spot/dipole axis and the rotation axis, and ψ the angle between the observer's direction and the rotation axis, then the angle α that the axis of the hot spot makes with respect to the line of sight to the observer can be written as

$$\alpha(t) = \arccos(\cos \psi \cos \xi + \sin \psi \sin \xi \cos \gamma(t)). \quad (2)$$

This angle is a function of the phase angle $\gamma(t) = \Omega(t)t$ swept by the star as it rotates with angular velocity $\Omega(t)$. The surface of the star is described by the angular spherical coordinates (θ, ϕ) , and the coordinate system is chosen so that the z axis coincides with the direction of the line of sight to the observer. The hot spot is described by the conditions:

$$\theta \leq \beta_h, \quad \text{if } \alpha = 0 \quad (3)$$

and

$$\begin{cases} \alpha - \beta_h \leq \theta \leq \alpha + \beta_h \\ 2\pi - \phi_p^h \leq \phi \leq \phi_p^h \end{cases} \quad \text{if } \alpha \neq 0 \quad \text{and} \quad \beta_h \leq \alpha \quad (4)$$

where

$$\phi_p^h = \arccos \left[\frac{\cos \beta_h - \cos \alpha \cos \theta}{\sin \alpha \sin \theta} \right]. \quad (5)$$

On the other hand, it is identified through the condition

$$\theta \leq \theta_*^h(\alpha, \beta_h, \phi), \quad \text{if } \alpha \neq 0 \quad \text{and} \quad \beta_h > \alpha, \quad (6)$$

where the outer boundary $\theta_*^h(\alpha, \beta_h, \phi)$ of the spot is computed by numerical solution of the equation

$$\cos \beta_h = \sin \theta_*^h \sin \alpha \cos \phi + \cos \theta_*^h \cos \alpha. \quad (7)$$

Due to the strong NS gravitational field, photons emitted at the NS surface suffer substantial deflection on their way to the observer. A photon emitted at a colatitude θ on the star makes an angle δ with the normal to the surface at the point of emission. The relation between δ and θ is given by the ray-tracing function¹ (Page 1995)

$$\theta(\delta) = \int_0^{R_s/2R} x \, du \left/ \sqrt{\left(1 - \frac{R_s}{R}\right) \left(\frac{R_s}{2R}\right)^2 - (1-2u)u^2x^2} \right., \quad (8)$$

having defined $x \equiv \sin \delta$. Here, R/R_s is the ratio between the NS and the Schwarzschild radius, $R_s = 2GM/c^2$ (we assume $M = 1.4M_\odot$).

A blackbody model for the local emission is assumed. While it would be desirable to perform this analysis with realistic magnetized atmosphere models, the lack of an extensive set of such models for high B -field strengths, ($B \geq 10^{14}$ G) and arbitrary inclinations (with respect to the NS surface) makes this more complete analysis not yet possible. This is particularly the case for the present study, since we are modeling the emission from the entire surface of the star, and over this there are large regions with a non-normal B . We note, however, recent work extending NS emission models to non-normal fields. In particular, LLoyd (2003a,b) presented model spectra for $B \leq 10^{14}$ G and for arbitrary orientation, for pure Hydrogen composition, and in the limit of complete ionization. Ho, Potekhin & Chabrier (2008) constructed partially ionized Hydrogen models for arbitrary field orientation and for

strengths in the range $10^{12} \leq B \leq 3 \times 10^{13}$ G. While these models are very useful for exploring NSs with moderate fields (e.g. Mori & Ho 2007), they are still not appropriate for the magnetic field strengths needed for a self-consistent modeling of XTE J1810-197 (B_{dip} of about 3×10^{14} G). Hence here we adopt the empirical approach of parameterizing the level of anisotropy with the function $f(\delta) \propto \cos^n \delta$ (since 'pencil' beaming dominates in atmosphere models), and perform the timing analysis with different values of n within a reasonable range as suggested by beaming in realistic descriptions of magnetized atmospheres².

The observed spectrum as a function of phase angle γ is then obtained by integrating the local emission over the observable surface of the star, including the effect of gravitational redshift of the radiation (Page 1995)

$$F(E_\infty, \gamma) = \frac{2\pi}{c h^3} \frac{R_\infty^2}{D^2} E_\infty^2 e^{-N_H \sigma(E_\infty)} \int_0^1 2x dx \times \int_0^{2\pi} \frac{d\phi}{2\pi} I_0(\theta, \phi) n[E_\infty e^{-\Lambda_s}; T(\theta, \phi)], \quad (9)$$

in units of photons $\text{cm}^{-2} \text{s}^{-1} \text{keV}^{-1}$. In the above equation, the radius and energy as observed at infinity are given by $R_\infty = R e^{-\Lambda_s}$, and $E_\infty = E e^{\Lambda_s}$, where R is the star radius, E is the energy emitted at the star surface, and Λ_s is defined through the relation

$$e^{\Lambda_s} \equiv \sqrt{1 - \frac{R_s}{R}}. \quad (10)$$

For the spectral function, given by $n(E, T) = 1/[\exp(E/kT) - 1]$, the temperature $T(\theta, \phi)$ is equal to T_h if $\{\theta, \phi\}$ satisfy any of the conditions (3) through (7), and it is given by $T(\theta, \phi) = T_{\text{th}}(\theta, \phi)$ otherwise. Correspondingly, the weighted intensity $I_0(\theta, \phi)$ is given by the beaming function $f[\delta(\theta)]$.

The phase-averaged flux is then readily computed as

$$F_{\text{ave}}(E_\infty) = \frac{1}{2\pi} \int_0^{2\pi} d\gamma F(E_\infty, \gamma). \quad (11)$$

Note that the phase dependence γ in Eq.(9) comes from the viewing angles implicit in $\alpha(t)$ and from the series of conditions (3) through (7).

We also included a multiplicative factor which accounts for the hydrogen column density between the observer and the star. Note that absorption does influence the predicted pulsed fractions, when these are computed over finite energy intervals (Perna et al. 2000). The magnitude of absorption was fixed to that obtained from the spectral fit (see §5.1). The model described in this section was imported into the spectral fitting package XSPEC (Arnaud 1996), and used to fit both spectra and pulse profiles.

¹ In the emission code, to improve the computational efficiency of the above equation, we use the approximation derived by Beloborodov (2002).

² In the magnetized atmosphere models by van Adelsberg & Lai (2006), the beaming strength depends on the magnitude of the B field, on the atmosphere temperature, on the observation energy, as well as on the angle δ itself. For fields and temperatures in the magnetar range, the models by van Adelsberg & Lai (2006) predict a strong forward beaming for angles $\delta \lesssim 40 - 60$ deg, and a much lower anisotropy level (fan-like) at larger angles. For example, for $B \sim 10^{14}$ G and $T \sim 0.4$ keV, an approximation to the intensity for $\delta \lesssim 50$ deg is $f(\delta) \propto \cos^{0.8} \delta$ at $E \sim 0.2$ keV, and $f(\delta) \propto \cos^2 \delta$ at $E \sim 1$ keV.

5 RESULTS

5.1 Spectral modeling

Fitting the phase averaged-spectrum with the model in Eq.(11) requires fixing the viewing angles ξ, ψ . However, since the viewing geometry is not known *a priori*, we followed an iterative procedure for our combined spectral and timing analysis. We start by assuming $\psi = \xi = 0$, the face-on geometry, with the observer looking directly down the co-aligned rotation axis and magnetic pole. This implies $\alpha = 0$ and speeds up the spectral fitting substantially as the geometric condition describing the hot spot (cfr. Eq. 3) depends only on the coordinate θ , reducing the flux integral in Eq.(9) to a single dimension. After fitting the phase-averaged spectrum, the spectral parameters are used to compute the pulse profiles for ξ, ψ ; this restricts the range of viewing angles ψ and ξ to those that best match the pulsed fractions. We then refit the phase-averaged spectrum to refine the spectral parameters, but now use the best ψ, ξ from the timing analysis. This procedure is iterated until the change in the parameters are consistent with the measurement errors. This procedure is found to converge in only one iteration and thus allows us to explore a wide grid of viewing angles (like e.g. in Gotthelf et al. 2010) in a reasonable time.

To begin with, the source distance was first fixed to $D=3.3$ kpc, based on radio pulse dispersion measure (Camilo et al. 2006), and consistent with the measurement derived from HI absorption ($D = 3.5 \pm 0.5$, Minter 2007) and the measurement derived from Red Clump Stars in the direction of the source ($D = 3.1 \pm 0.5$ Durant & van Kerkwijk 2006). For completeness, we then also studied the cases corresponding to the distance fixed at 2 kpc and 5 kpc, which correspond to the borderline values of the 3σ uncertainty on the distance. All the fits were performed in the 0.5–3 keV spectral band. Above 3 keV, source detection is not significant. We repeated the spectral analysis for several values of the beaming parameter n (in the range 0 – 2.5, using steps of 0.5), and found that, within the measurement uncertainties, the inferred spectral parameters were all consistent. Hence, for the spectral analysis, we set $n = 0$.

Like in the case of the analysis performed by Perna & Gotthelf (2008), an important technical issue for these fits is the degree of degeneracy between the radius R and the variable parameters, in this case (kT_h, β_h, kT_p). Without fixing the radius and the distance there is no unique solution, and we considered a range of possible values, $9 \leq R \leq 15$ km, in 1 km increments, for the radius, and the above 3σ range of $2 \leq D \leq 5$ kpc.

For the distance values of $D = 3.3$ kpc and $D = 2$ kpc, over the sampled range of radii, spectral analysis provides acceptable fits, but did not allow a preferred radius based on the χ^2 measurement (see table 1). In the case of $D = 5$ kpc, spectral fits showed a significantly higher χ^2 value, ranging from 1.4 (for $R = 15$ km) to 2.04 (for $R = 9$ km). These fits resulted to be statistically unacceptable; consequently, the timing analysis described in the following is only performed for $D = 3.3$ kpc and $D = 2$ kpc.

5.2 Pulsed fraction and pulse profile modeling

Given the smooth and nearly sinusoidal pulse shape, the pulsed fraction (PF) of the signal has been determined using the expression

$$\text{PF} = \frac{F_{\text{max}} - F_{\text{min}}}{F_{\text{max}} + F_{\text{min}}} \quad (12)$$

Fluxes are integrated over the given energy bands. In the adopted geometry, the maximum and minimum fluxes of the model, F_{max}

and F_{min} , correspond to phases $\gamma = 0$ and $\gamma = \pi$, respectively. As discussed in §3, this is true for any combination of viewing angles in the higher energy bands ≥ 1 keV, in which the emission is either dominated, or largely influenced, by the (single) hot spot. In the lowest energy band (0.5–1 keV), where the contribution from the surface emission is dominant, a single peak can only be obtained for viewing angles $\xi, \psi \lesssim \xi_{\text{max}}, \psi_{\text{max}}$. The latter depend mildly on n, R , and are generally $\lesssim 50^\circ - 55^\circ$. Our viewing parameter search is restricted to the range of angles for which the lowest energy band remains single peaked. Incidentally, the high ξ, ψ parameter range is also *independently* ruled out by the PF in the highest energy band alone: for most combinations of n, R , the predicted PF would be much higher than the measured value.

A measure of the PF in each energy interval was obtained using the timing solution, phase-connecting the three pointings. The background level, which was variable during the three pointings, was subtracted for each multi-instrument lightcurve. We found that the PF increases with energy: $\text{PF}_{(0.5-1 \text{ keV})} = 17 \pm 1\%$, $\text{PF}_{(1-1.5 \text{ keV})} = 26 \pm 0.8\%$, $\text{PF}_{(1.5-2 \text{ keV})} = 36 \pm 1.3\%$, $\text{PF}_{(2-3 \text{ keV})} = 47 \pm 2.6\%$ (all the uncertainties are hereafter reported at 1σ confidence level, c.l., unless otherwise stated). Above 3 keV, due the low S/N ratio, only an upper limit on the PF could be obtained (but this is not an useful value for the purpose of this work). Hence our timing analysis uses the data up to 3 keV.

Starting with the best spectral fit model parameters presented in Table 1, obtained for $\psi = \xi = 0$, the best values of ψ^* and ξ^* needed to reproduce the observed pulsed fraction were searched (in the case of $D=3.3$ kpc and $D=2$ kpc). Given the high S/N of the data, both the pulsed fraction and the full pulse profile were modeled.

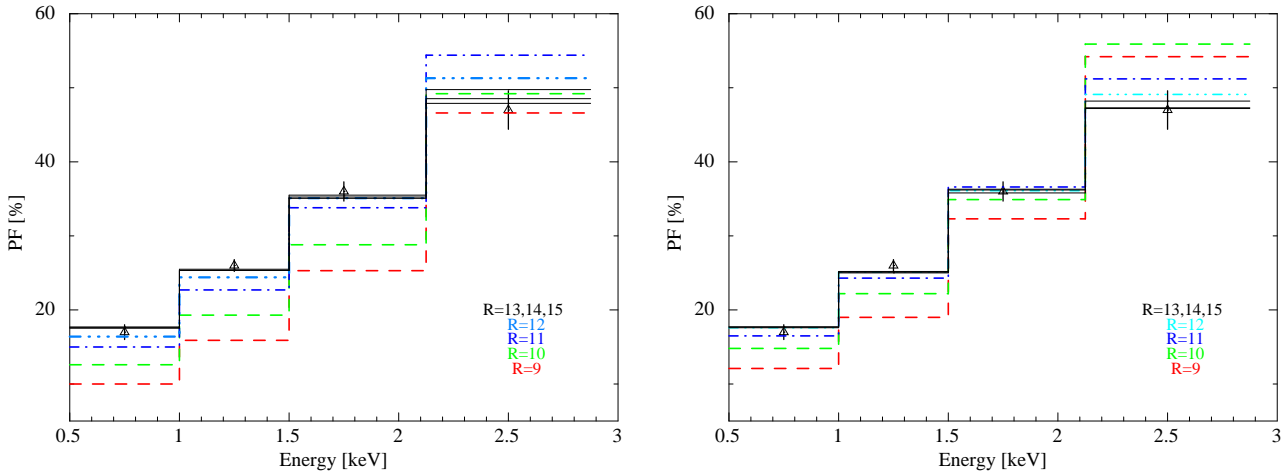
For each value of the NS radius fitted for in §5.1 (9–15 km), the pulsed fraction, defined in Eq.(12), was computed over the grid of angles $(\xi, \psi) \leq (\xi_{\text{max}}, \psi_{\text{max}})$ deg, in 1 degree intervals. For each value on the grid, the model predictions were compared with data. Notice that the flux depends on the angles ξ and ψ only through the parameter α in Eq.(2), and therefore it is symmetric with respect to an exchange of ξ and ψ .

In order to explore the behaviour of the PF with both R and n independently, we first examined how the PF varied with R at fixed n , and then how they varied with n at fixed R . In the following, we first report the results for $n = 1$ and $R = 9 - 15$ km, in steps of 1 km and then for $R = 9$ km and $R = 15$ km, for $n = 0 - 2.5$, in steps of 0.5. The behaviour for other combinations of parameters can then be inferred from the results shown.

For the case $n = 1$, Table 2 reports the best geometry (expressed through the angles ψ^* and ξ^*), for each sampled radius, and the corresponding predicted PF as a function of the energy band, in comparison with the data. For this case, we further explored the dependence of the results on the source distance. In the case of $D = 3.3$ kpc, low radius values ($9 \leq R \leq 12$ km), underpredict the observed PF for low energy intervals $0.5 \leq E \leq 2$ keV. Moreover, for $R = 11$ and $R = 12$ km, the model overpredicts the observed PF in the highest energy band ($2 \leq E \leq 3$ keV; see 3). The different trend of the PFs with radius in the low and high energy bands is due to the fact that the flux in these is dominated by different components: the cooler component from the all NS surface in the low energy band, and the hotter small spot in the high energy band. The smooth temperature gradient of the former makes the PFs less sensitive to changes in the viewing geometry, and hence the dominant factor in determining the change in the PF with R is the general-relativistic suppression of the pulsed fraction as R decreases. On the other hand, the pulsed fraction produced by the small hot spot is much more sensitive to changes in viewing

Table 1. Spectral fit parameters as a function of the radius R . 1σ c.l. uncertainty is reported.

$D = 3.3$ kpc					
R km	nH $\times 10^{21} \text{ cm}^{-2}$	kT_{BB} keV	kT_{p} keV	β_{h} deg	χ_{red}^2 (for 75 d.o.f.)
9	6.9 ± 0.1	0.57 ± 0.02	0.267 ± 0.001	$2.1^{+0.1}_{-0.3}$	1.42
10	7.1 ± 0.1	0.54 ± 0.02	0.250 ± 0.001	1.8 ± 0.4	1.34
11	7.3 ± 0.1	0.52 ± 0.03	0.238 ± 0.002	$2.0^{+0.6}_{-0.1}$	1.28
12	7.4 ± 0.1	0.47 ± 0.01	0.226 ± 0.001	$2.4^{+0.1}_{-0.7}$	1.22
13	7.5 ± 0.1	0.45 ± 0.01	0.218 ± 0.001	$2.0^{+0.3}_{-0.5}$	1.17
14	7.7 ± 0.1	0.44 ± 0.01	0.211 ± 0.001	2.1 ± 0.3	1.13
15	7.8 ± 0.1	0.43 ± 0.01	0.205 ± 0.001	$2.2^{+0.1}_{-0.2}$	1.10
$D = 2.0$ kpc					
9	7.9 ± 0.1	0.48 ± 0.01	0.235 ± 0.001	2.6 ± 0.2	1.08
10	8.1 ± 0.1	0.452 ± 0.003	0.221 ± 0.001	$2.2^{+0.6}_{-0.1}$	1.06
11	8.2 ± 0.1	0.43 ± 0.03	0.211 ± 0.002	$2.5^{+0.2}_{-0.1}$	1.03
12	8.4 ± 0.1	0.416 ± 0.003	0.202 ± 0.001	2.2 ± 0.2	1.02
13	8.5 ± 0.1	0.403 ± 0.002	0.194 ± 0.001	2.4 ± 0.3	1.01
14	8.7 ± 0.1	0.391 ± 0.002	0.188 ± 0.001	$2.1^{+0.6}_{-0.1}$	1.00
15	8.8 ± 0.1	0.383 ± 0.002	0.183 ± 0.001	$2.0^{+0.8}_{-0.1}$	1.00

**Figure 3.** Model predicted PF (for the best emission geometry as reported in Table 2) for different radius values, compared with data. Left panel is for $D = 3.3$ kpc, while right panel is for $D = 2.0$ kpc. Beaming factor is equal to 1. Dashed and dot-dashed lines represent the model prediction for low radius values ($9 \leq R \leq 12$ km), while continuous black lines are obtained for high radius values ($13 \leq R \leq 15$ km). 1σ c.l. uncertainty is reported.

angles with the result that smaller R 's, which are best fit by larger values of ξ, ψ (see Table 2), yield higher PFs. We found that it is not possible to reproduce the observed pulsed fraction for low radius values ($9 \leq R \leq 12$ km), which are hence rejected by the model for this distance. The predicted PF for high radius values ($13 \leq R \leq 15$ km) is instead fully consistent with the data, within 1σ uncertainty. Figure 3 shows the model predicted PF, for all the values of the radii considered, compared with the data. Similar results are obtained for $D = 2$ kpc; however in this case the range of allowed radii is wider, including also $R = 12$ km. For, e.g., an intermediate value of the radius, $R = 13$ km ($D = 3.3$ kpc), the best viewing geometry angles range from $\psi^* = \xi^* = 38^\circ$ to $(\psi, \xi) = (52^\circ, 29^\circ)$ at 3σ c.l. (see Table 2). The angles (ψ, ξ) that provide the best match to the PF data clearly vary with R , for a

fixed value of the beaming factor n . Smaller radii require a larger variation in $\alpha(t)$ (α varies between $\psi - \xi$ and $\psi + \xi$) to compensate for the stronger general-relativistic suppression of the flux modulation.

The χ^2_{red} map, computed for both the case of $R = 9$ km and $R = 14$ km (Figure 4), displays the 68%, 90% and 99% confidence levels. This map is produced by comparing the model and observed pulsed fraction over a range of possible (ξ, ψ) angle pairs, for our best fit spectral model parameters. The viewing geometry was found to be well constrained, with the range of allowed 3σ solutions a factor of 2.5 smaller than (but consistent with) what was found by Perna & Gotthelf (2008) in the analysis of the outburst decay (where the 3σ c.l. of the viewing parameters were ranging from $\psi^* = \xi^* = 37^\circ$ to $\psi, \xi = 85^\circ, 15^\circ$). This consistency is

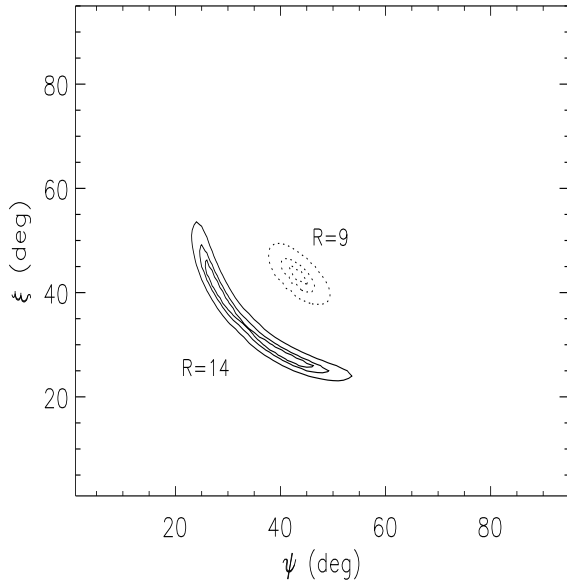


Figure 4. Reduced chi-square (χ^2_{ν}) maps obtained by comparing data and model pulsed fraction described in the text for a range of viewing angles ψ and ξ . The 68%, 90% and 99% confidence levels are shown for the best match to the observed pulsed fractions using the beaming pattern $n = 1$ for $R = 9$ km and $R = 14$ km. The results are clearly degenerate with respect to an interchange of (ξ, ψ) . A comparison with Fig. 2 in Perna & Gotthelf (2008) shows the substantial reduction in the confidence range.

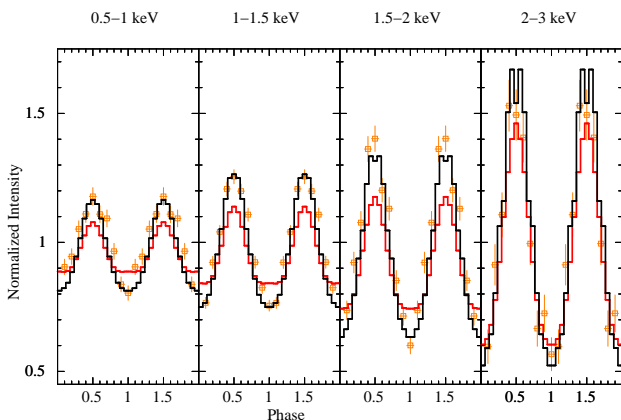


Figure 5. Predicted pulse profile for $R = 13$ km (black line), and $R = 9$ km (red line), $D = 3.3$ kpc and $n = 1$, in four energy bands, compared to data (orange squares). The two cases $R = 14$ and $R = 15$ km give fully consistent results with $R = 13$ km. Each profile is computed with the best fit viewing angles as reported in Table 2.

not surprising, since the warm spot appears to be the remnant of the heated regions during the outburst. The elongated shape of the contour plots shows that the two angles ψ and ξ are highly correlated in the fit. This is a result of the fact that the PF depends on a combination of these two angles.

Having assumed a face-on spectrum to derive the spectral model parameters used to compute the pulsed fractions, we now proceeded to refit the spectrum, for each radius, using the best viewing geometry ψ^*, ξ^* . This is iterated to a convergence crite-

ria set by the measurement errors. The final spectral values in all cases are consistent with those found for $\psi = \xi = 0$. (Table 1). For example, for the special cases of $R = 13$ km, $D = 3.3$ kpc, and $\psi^* = 38^\circ$ and $\xi^* = 38^\circ$, we find $n_H = 7.5 \pm 0.1$, $kT_{\text{BB}} = 0.453 \pm 0.003$, $kT_p = 0.218 \pm 0.001$ and $\beta_h = 2.0 \pm 0.1^2$, with $\chi^2 = 87.7$ for 75 d.o.f. (see Figure 7); as another example, for $R = 13$ km, $D = 2.0$ kpc, and $\psi^* = 42^\circ$ and $\xi^* = 28^\circ$, we find $n_H = 8.4 \pm 0.1$, $kT_{\text{BB}} = 0.413 \pm 0.003$, $kT_p = 0.24 \pm 0.03$ and $\beta_h = 2.0 \pm 0.1^2$, with $\chi^2 = 76.4$ (for 75 d.o.f.). Given the consistency between the spectral parameters determined with $\psi = \xi = 0$ and with those for the best viewing angles ψ^*, ξ^* , the iterative process did not need to be continued further. For the best fit spectral parameters and viewing angles, the resulting pulsed fractions and pulse profile, for several radii, are shown in Figure 3 and 5, respectively. It is important to note that, for a pre-determined emission pattern of the radiation (here parameterized by the beaming parameter n), there are values of radii (e.g., $R \leq 12$ km for $n = 1$) for which no good solution to the combined spectral/timing properties of the source can be found. Hence this type of analysis provides useful limits on the NS radius in the context of the model.

To consider the effect of the angular distribution of radiation on our spectral and timing modeling, we repeated the above analysis for various assumed beaming indexes. Table 3 reports the model predicted PF for $0 \leq n \leq 2.5$, in 0.5 step increments, for $R = 9$ km and $R = 15$ km (see Figure 6). For $n = 0$ (isotropic emission), we found that not even the largest radii were able to account for the observed level of modulation. The modeled PF is, in fact, produced by the interplay of two flux components: the one from the whole NS surface, and the other from the small, hot spot. The high level of pulsation which could have been produced by the hot component alone, is strongly reduced by the presence of emission on the entire NS surface. If the local emission is isotropic, not even the largest radii can provide sufficiently large PFs. However, as the value of n increases, the range of allowed radii becomes wider; we found that for $n = 0.5$, only $R = 15$ km provides a marginal match for the energy-dependent PF; for $n = 1$, the range $R \geq 13$ km provides a good overall representation of the data. For $n = 2.5$, due to the resulting strong increase of the PF at all energies, a good match to the PFs can be found for each value of R (but clearly for different combinations of the angles ψ, ξ). While our results provide a hint to the presence of a magnetized atmosphere on the NS surface, they also show that without a priori knowledge of $f(\delta)$ for each (θ, ϕ) on the NS surface, the timing analysis does not allow to break the degeneracy with the radius (at least within our measurement uncertainties).

6 SUMMARY AND DISCUSSION

The decline of the post-outburst emission of XTE J1810–197 has allowed us to perform a detailed spectral and timing analysis of the emission of this source in its quiescent state. The main results from the modeling described herein can be summarized as follows:

(i) The temperature distribution on the surface of the NS is consistent with the expectations of a dipole magnetic field configuration. We remark that our analysis does not guarantee that a dipolar magnetic field represents the only possible solution; in principle, other magnetic field configurations and beaming patterns can be ad-hoc produced and tested for this source. However, a dipolar field is the simplest magnetic field configuration for a pulsar, and one that yields a single peak, nearly sinusoidal (as observed in XTE J1810–197), for a wide range of viewing angles. Hence,

Table 2. Best emission geometry angles ψ^* and ξ^* and corresponding predicted pulsed fraction, for $n = 1$ and variable R , compared to the data. 1σ c.l. uncertainty is reported

$D = 3.3$ kpc					
R km	PF _{0.5÷1 keV} %	PF _{1÷1.5 keV} %	PF _{1.5÷2 keV} %	PF _{2÷3 keV} %	ψ^*, ξ^* degree
9	10.0	15.7	24.9	45.8	48,48
10	12.6	19.3	28.8	49.2	46,46
11	15.0	22.7	33.8	54.4	44,44
12	16.6	24.7	35.6	52.1	40,39
13	17.5	25.3	34.9	49.8	38,38
14	17.5	25.2	34.8	48.1	40,31
15	17.7	25.4	35.3	47.8	41,28
$D = 2.0$ kpc					
9	12.1	19.0	32.3	54.2	46,46
10	14.8	22.2	34.9	55.9	44,44
11	16.5	24.3	36.6	51.2	39,38
12	17.6	25.1	36.1	49.1	37,36
13	17.6	25.2	36.3	47.2	41,28
14	17.7	25.1	36.2	48.2	45,25
15	17.7	25.0	35.8	47.3	46,23
observed PF	17 ± 1.0	26.0 ± 0.8	36 ± 1.3	47 ± 2.6	

Table 3. Best emission geometry angles ψ^* and ξ^* and corresponding predicted pulsed fraction, for different value of the beaming factor n and $D = 3.3$ kpc, compared to data. 1σ c.l. uncertainty is reported

$R = 9$ km					
n	PF _{0.5÷1 keV} %	PF _{1÷1.5 keV} %	PF _{1.5÷2 keV} %	PF _{2÷3 keV} %	ψ^*, ξ^* degree
0.0	0.7	2.0	6.4	23.2	55,55
0.5	5.3	9.0	16.1	35.6	50,50
1.0	10.0	15.7	24.9	45.8	48,48
1.5	14.1	21.8	32.4	52.8	45,45
2.0	16.5	24.9	35.0	51.1	39,38
2.5	17.1	25.4	35.1	49.2	37,31
$R = 15$ km					
0.0	8.8	14.4	26.1	51.7	51,48
0.5	15.9	23.5	34.8	52.5	42,41
1.0	17.7	25.4	35.3	47.8	41,28
1.5	17.6	25.3	35.3	47.7	44,21
2.0	17.4	25.0	35.0	47.2	43,18
2.5	17.6	25.2	35.3	47.5	38,18
observed PF	17 ± 1.0	26.0 ± 0.8	36 ± 1.3	47 ± 2.6	

although not formally unique from a mathematical point of view, the proposed solution is physically motivated, and the fact that it provides such a good match to the data yields confidence that it is indeed a reasonably good representation of the quiescent emission of this transient magnetar.

(ii) The pulsed fraction of the NS emission requires an anisotropic, pencil-type radiation pattern, which is a likely indication of the presence of a magnetized atmosphere on the NS surface. For a $\cos^n \delta$ emission profile, we performed a timing analysis for

n in the range 0-2.5 (in steps of 0.5), and radii between 9-15 km (in steps of 1 km). We found that no match to the PF data could be obtained for $n = 0$ (isotropic radiation pattern), no matter the value of the radius, while for $n = 2.5$, a good match to the PFs could be found even for $R = 9$ km (smaller values of the radius are increasingly allowed as n increases). For each value of n in between there is a range of radii which are not allowed by the PF data (e.g. for $n = 1$ no good match could be found for $R \leq 12$ km). Therefore, our analysis has clearly demonstrated how a detailed a

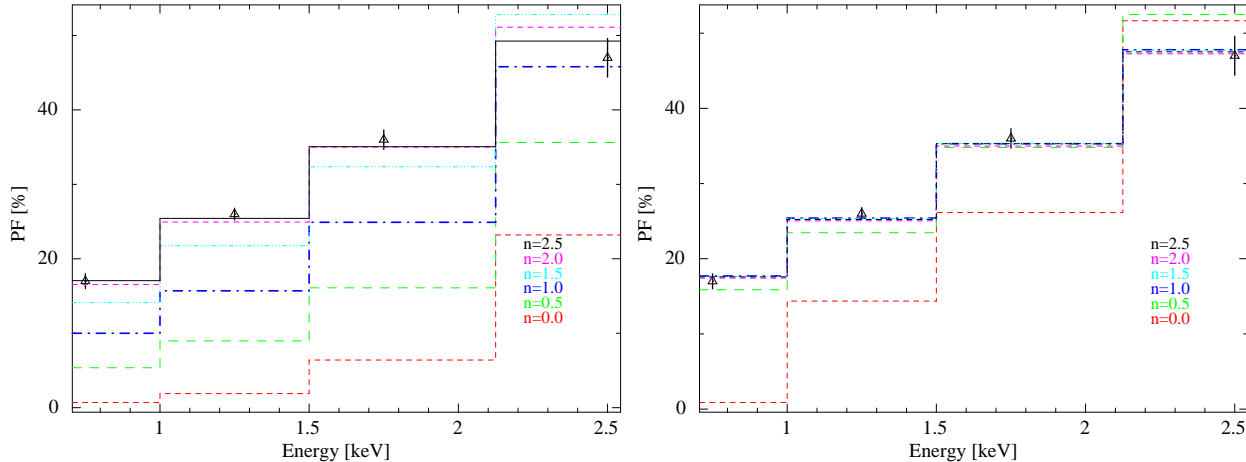


Figure 6. Model predicted PF (starting from the best emission geometry as reported in Table 3) for different values of the beaming pattern n . Left panel is for $R=9$ km, while right panel is for $R=15$ km. 1σ c.l. uncertainty is reported.

priori knowledge of the spectral distribution and emission pattern as a function of (θ, ϕ) on the entire surface of the star has the power to allow a radius constraint for the NS.

(iii) The overall emission geometry is constrained by identifying likelihood regions in the $\psi - \xi$ parameter space. The most significant range according to our fits is consistent with the results of the earlier, post-outburst analysis of Perna & Gotthelf (2008), but the 3σ allowed region is now reduced by a factor of 2.5. We note that the hot-spot axis used in the earlier work coincides with the dipole axis in the current study.

A spectral and timing analysis of the post-outburst emission of XTE J1810–197 has been performed also by Albano et al. (2010). They fitted the first 7 observations using a three-temperature model. The X-ray emission is produced in a globally twisted magnetosphere, and parameterized by the twist angle, the electron velocity and the seed photon temperature. In the last two sets, the flux is approaching the quiescent level, and only two temperatures are required to fit the X-ray spectrum. For these observations, they found that the angle between the magnetic axis and the rotation axis is $\xi = 30.0^{\circ} +12.3_{-20.0}$ in the 6th observation, and $\xi = 22.7^{\circ} +16.4_{-20.0}$ in the 7th, 6 months later, while the angle between the line of sight and the rotation axis was found to be $\psi = 153.9^{\circ} +19.6_{-16.0}$ in the 6th and $\psi = 145.8^{\circ} +16.4_{-9.5}$ in the 7th observation. While the values of the angle ξ are roughly within the range of what we find, the angle ψ is inconsistent with ours. A direct comparison between our modeling and theirs is however not possible due to some fundamental differences in the basic assumptions. Our quiescent emission is assumed to be thermal, and we leave the anisotropy level of the local radiation as a free parameter. On the other hand, the twisted magnetosphere model has a well determined angular radiation pattern. The NS surface temperature is assumed to follow a dipolar-like pattern in our model, while in theirs it is assumed to be constant. Furthermore, our modeling includes the general relativistic effect of light deflection (which heavily influences the pulsed fractions and hence the viewing geometry that we infer), while their modeling does not.

Our study has allowed us to establish some important properties of the quiescent emission of XTE J1810–197. The spectral analysis has shown evidence for the presence of a very small hot spot, only a couple of degrees in size. This emission component dominates the X-ray flux above about 1 keV. Interestingly,

a small hot region is also characteristic of the quiescent emission of another (transient) AXP, CXOU J164710.2–455216 (Israel et al. 2007; Skinner et al. 2006). The most natural interpretation, in the case of XTE J1810–197 as well as in the case of CXOU J164710.2–455216, is the association of this warmer region to a concentration of magnetic field lines, since the surface heat flux of a magnetar scales sensitively as $B^{4.4}$ (Thompson & Duncan 1996). It is then not surprising that this region coincides with the location of the outburst, as our analysis for XTE J1810–197 has shown.

Our constraints on the viewing geometry could in principle be combined with those obtained from radio measurements following the outburst, to further restrict the allowed parameter space. Camilo et al. (2007a) showed that the radio and X-ray locations were aligned, within some rather large uncertainty due to the small number of counts of their *Chandra* data. Camilo et al. (2007b) used radio polarimetry to fit for the angle angle between the magnetic field and the rotation axis (ξ in our notation), and for the angle between the magnetic field axis and the line of sight ($\alpha_{min} = \psi - \xi$ in our notation), finding two possible configurations: one with $\xi = 70^{\circ}$ and $\alpha_{min} \sim 20^{\circ} - 25^{\circ}$, and another with $\xi = 4^{\circ}$ and $\alpha_{min} = 4^{\circ}$. Polarization observations of XTE J1810–197 were also used by Kramer et al. (2007) to constrain the viewing geometry of this pulsar. They identified a main pulse and a mid pulse, produced in different locations on the star. Their best fitted angles (with the same notation as above) were $\xi = 44^{\circ}$ and $\alpha_{min} = 39^{\circ}$ for the main pulse, and $\xi = 76^{\circ}$ and $\alpha_{min} = 6^{\circ}$ for the inter pulse. Given some discrepancies between the different angle estimates from radio data, and the lack of a firm and accurate association between the radio and X-ray emitting regions, we refrain in the current work from using the radio angle determinations to restrict our allowed parameters range. However, we take the opportunity to emphasize the importance of simultaneous radio-X ray observations should another outburst occur (either in this or in another magnetar).

Our analysis has allowed us to explore the consistency of the data with the expectations for the temperature distribution on the NS surface if the B field is dominated by a dipolar component. The angles ξ and ψ that provide a good match to the observed pulsed fractions (Fig. 3 and Table 2) also ensure that the profile remains single-peaked in the lowest energy band, dominated by the surface/dipolar component. Combinations of the beaming parameter and the NS radius can be found for which our model provides an

excellent match to spectra, pulsed fractions and, more generally, to the full pulse profile. Within the context of magnetars, being able to infer the magnetic topology is important for a number of reasons. Firstly, measurements of the magnetic field strength from P and \dot{P} make the implicit assumption of a dipolar field; substantial departures from this configuration will result in biased estimates. Second, the magnetic field topology in magnetars also plays an important role in the resulting outbursting behaviour (Thompson & Duncan 1995, 1996), in that it regulates the intensity, frequency and location on the NS surface of the starquakes, and hence of the outbursts (Perna & Pons 2011).

Ultimately, we note how the combined spectral/timing analysis that we performed has the potential to constrain the compactness ratio of the neutron star (or equivalently the radius, for a given mass). However, obtaining this type of constraint requires an a priori knowledge of the spectral and radiation pattern of the local emission. This is particularly difficult in the case of highly magnetized objects, since the local emission depends on the local strength and orientation of the B field, which in turn would need to be determined as a part of the fitting procedure. This analysis, which has begun for NSs with magnetic fields in the $10^{12} - 10^{13}$ G range (Ho & Mori 2008), will become possible for magnetars once atmospheric models for arbitrary field orientations (Lloyd 2003a,b; Ho et al. 2007) are extended to strengths $B \sim 10^{14} - 10^{15}$ G.

ACKNOWLEDGEMENTS

Federico Bernardini thanks Prof. Svetozar Zhekov for his precious help. This work was partially supported by grants nsf-ast 1009396, NASA NNX10AK78G, NNX09AT17G, NNX09AT22G, NNX09AU34G, GOO-11077X, DD1-12052X, G09-0156X, AR1-12003X, DD1-12053X (RP).

REFERENCES

- Albano, A., Turolla, R., Israel, G. L., et al. 2010, *ApJ*, 722, 788
 Arnaud, K. A. 1996, *Astronomical Data Analysis Software and Systems V*, 101, 17
 Beloborodov, A. M. 2002, *ApJ*, 566, L85
 Bernardini, F., Israel, G. L., Dall’Osso, S., et al. 2009, *A&A*, 498, 195
 Camilo, F., Ransom, S. M., Halpern, J. P., et al. 2006, *Nature*, 442, 892
 Camilo, F., Cognard, I., Ransom, S. M., et al. 2007, *ApJ*, 663, 497
 Camilo, F., Reynolds, J., Johnston, S., et al. 2007a, *ApJ*, 659, L37
 Camilo, F., Ransom, S. M., Pealver, J., et al. 2007b, *ApJ*, 669, 561
 Dall’Osso S., Israel, G. L., Stella, L., et al. 2003, *ApJ*, 599, 485
 DeDeo, S., Psaltis, D., & Narayan, R. 2000, *Rossi2000: Astrophysics with the Rossi X-ray Timing Explorer*,
 Duncan, R. C., & Thompson, C. 1992, *ApJ*, 392, L9
 Durant, M., & van Kerkwijk, M. H. 2006, *ApJ*, 650, 1070
 Gotthelf, E. V., Halpern, J. P., Buxton, et al. 2004, *ApJ*, 605, 368
 Gotthelf, E. V., & Halpern, J. P. 2005, *ApJ*, 632, 1075
 Gotthelf, E. V., & Halpern, J. P. 2007, *Ap&SS*, 308, 79
 Gotthelf, E. V., Perna, R., & Halpern, J. P. 2010, *ApJ*, 724, 1316
 Halpern, J. P., & Gotthelf, E. V. 2005, *ApJ*, 618, 874
 Helfand, D. J., Chatterjee, S., Briskin, et al. 2007, *ApJ*, 662, 1198
 Heyl, J. S. & Hernquist, L. 1998, *MNRAS*, 300, 599
 Ho, W. C. G., Potekhin, A. Y., & Chabrier, G. 2008, *ApJS*, 178, 102
 Ho, W. C. G. & Mori, K. 2008, *AIP Conf. Proc.*, Vol. 983, pp. 340
 Ibrahim, A. I., Markwardt, C. B.; Swank, J. H., et al. 2004, *ApJ*, 609, L21
 Israel, G. L., Campana, S., Dall’Osso, S., et al. 2007, *ApJ*, 664, 448
 Kramer, M., Stappers, B. W., Jessner, A., et al. 2007, *MNRAS*, 377, 107
 Lloyd, D. 2003a, PhD Thesis, Harvard University, Source DAI-B 64/05, p. 2228
 Lloyd, D. A. 2003b, arXiv:astro-ph/0303561
 Mereghetti, S. 2008, *A&A Rev.*, 15, 225
 Minter, A. H. 2007, *SINS - Small Ionized and Neutral Structures in the Diffuse Interstellar Medium*, 365, 74
 Mori, K. & Ho, W. 2007, *MNRAS*, 377, 905
 Page, D. 1995, *ApJ*, 442, 273
 Pechenick, K.R., Ftaclas, C., & Cohen, J. M. 1983, *ApJ*, 274, 846
 Perna, R., Heyl, J., & Hernquist, L. 2000, *ApJ*, 538, L159
 Perna, R., Heyl, J. S., Hernquist, L. E., et al. 2001, *ApJ*, 557, 18
 Perna, R., & Gotthelf, E. V. 2008, *ApJ*, 681, 522
 Perna, R., & Pons, J. A. 2011, *ApJ*, 727, L51
 Skinner, S. L., Perna, R., & Zhekov, S. A. 2006, *ApJ*, 653, 587
 Strüder, L., Briel, U., Dennerl, K., et al. 2001, *A&A*, 365, L18
 Thompson, C., & Duncan, R. C. 1995, *MNRAS*, 275, 255
 Thompson, C., & Duncan, R. C. 1996, *ApJ*, 473, 322
 Turner, M. J. L., Abbey, A., Arnaud, M., et al. 2001, *A&A*, 365, L27
 van Adelsberg, M., & Lai, D. 2006, *MNRAS*, 373, 1495

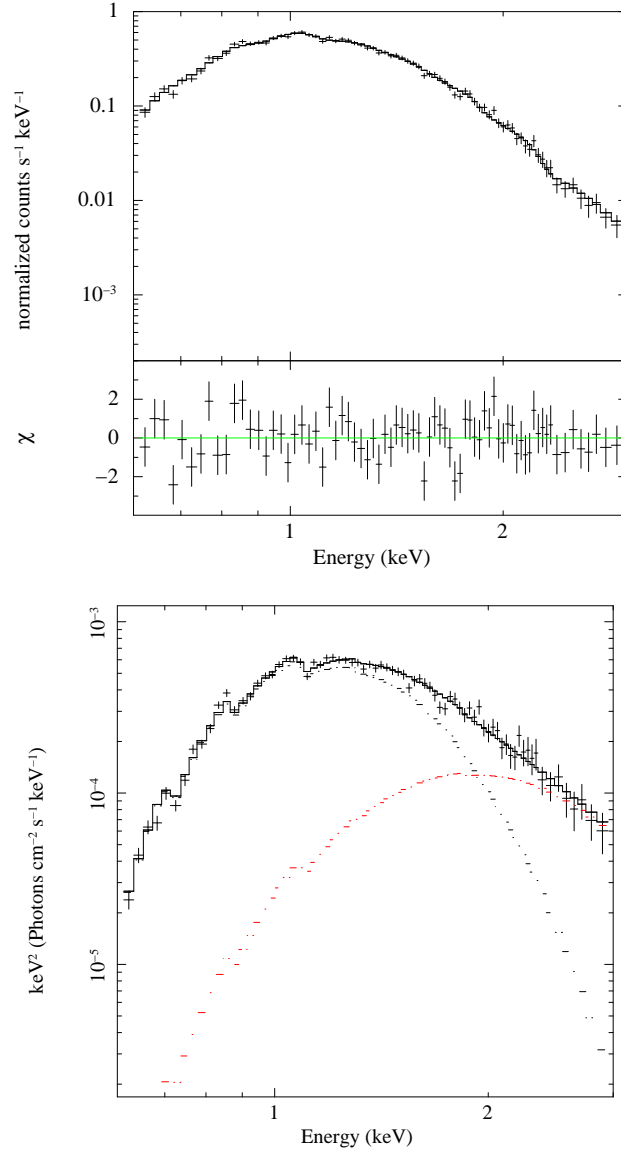


Figure 7. *Upper panel:* XMM-Newton phase-averaged spectrum of XTE J1810–197 obtained with the model presented in the text, for the specific case of $R=13$ km, $D=3.3$ kpc, and the best fit angles $\psi^* = 38^\circ$ and $\xi^* = 38^\circ$. Model residuals are shown in the lower panel. The parameters for the best fit model are reported in Table 1. The data show the summed spectra from the three observations. *Lower panel:* Same as the upper panel, but for unfolded source spectra. The contribution of the different model component is also shown: surface (black dotted line), warm spot (red dotted line).